Suppression of Secondary Diffraction Maxima via Binarized Cosine Window Transmission Gratings

Jian Yu(俞健)[1], Run-Xiang Xia(夏润翔)[1], Yan-Meng Dai(代艳萌)[1], Di-Kai Li(李迪开)[1], Qian Chen(陈前)[1], Jia-Qiang Zou(邹家强)[1], Shao-Xuan Cui(崔少轩)[1], Lei-Feng Cao(曹磊峰)[1,†], Cang-Tao Zhou(周沧涛)[1] and Shuang-Chen Ruan(阮双琛)[1]

[1]*Center for Intense Laser Application Technology, College of Engineering Physics,Guangdong Engineering Technology Research Center for High-Power Ultrafast Laser and X-Ray Equipment, Shenzhen Technology University, Shenzhen 518118, China*

Transmission gratings are widely used in soft X-ray spectroscopy for laser–plasma diagnostics due to their structural simplicity, moderate spectral resolution, and broad bandwidth. However, secondary diffraction maxima located between the principal orders introduce spectral contamination and degrade measurement accuracy. In this work, we propose a binarized cosine window to replace conventional rectangular slit apertures in transmission gratings. Through theoretical analysis, numerical simulations, and visible-light experiments, we demonstrate that the proposed design effectively redistributes diffracted energy from secondary maxima into the principal maxima. Experimental results show a reduction of 93.12% in secondary peak intensity and an improvement of approximately 27.36 dB in signal-to-noise ratio. This suppression mechanism enhances both spectral resolution and measurement reliability, providing a practical approach for improving soft X-ray spectroscopic diagnostics. The proposed method offers a promising pathway for high-precision spectral analysis in applications such as high energy density physics and advanced materials research.

Keywords: Transmission Gratings, Secondary Diffraction Suppression, Cosine Modulation, Binarization.

PACS: 42.79.Ci, 42.25.Fx, 07.85.Fv

1. Introduction

Transmission grating (TG) spectrometers are widely employed across astronomy, physics, materials science, environmental monitoring, and biomedicine due to their broad spectral coverage and structural simplicity[1-7]. In astronomical observations, TGs enable the spectral characterization of stellar coronae and interstellar media[8, 9], while in high energy density physics (HEDP) experiments such as inertial confinement fusion (ICF) diagnostics, they serve as essential tools for resolving the emission spectra of laser-produced plasmas[10]. TGs consist of periodic parallel slits that spatially separate wavelengths through diffraction[11, 12]. In the soft X-ray regime (0.1–10 nm)[13], reflective optics become inefficient and conventional refractive elements are impractical, making transmission-based diffractive elements the preferred choice[14]. However, precise fabrication via lithography and etching is essential for achieving adequate transmission and spectral performance[15, 16].

† Corresponding author. E-mail: caoleifeng@sztu.edu.cn

The diffraction pattern of a transmission grating arises from the convolution of its periodic structure with the aperture function[17-19]. The resulting Fourier spectrum encodes wavelength and intensity information for spectral analysis. Principal maxima occur at angles satisfying the grating equation $d\sin\theta=m\lambda$, where d is the grating constant, θ is the diffraction angle, m is the diffraction order, and λ is the wavelength[20]. First-order diffraction is typically employed for measurements due to its optimal balance between efficiency and dispersion, whereas zero-order lacks spectral information and higher orders are too weak[21-23].

However, secondary diffraction peaks appear between principal orders due to incomplete destructive interference and sidelobe overlap[24-27]. Although weaker than principal maxima, these secondary peaks introduce spectral contamination that degrades resolution and accuracy, particularly in high-sensitivity measurements or with spectrally dense sources[28, 29]. In practice, such contamination can cause spectral lines from different elements to overlap, leading to erroneous identification of elemental composition or inaccurate temperature and density diagnostics in plasma experiments[30, 31]. Suppressing secondary peaks is therefore essential for improving grating-based spectroscopy[32].

Concepts developed in visible optics are often transferable to X-ray systems. For example, soft-edge apertures can suppress side lobes, reducing secondary diffraction features. In the signal processing domain, windowing functions such as the Hanning, Hamming, and Blackman windows are routinely applied to reduce spectral leakage in discrete Fourier transform analysis[33, 34]. The underlying principle is that a smooth, tapered envelope in the spatial (or temporal) domain produces a narrower main lobe and suppressed sidelobes in the frequency domain[35]. Similarly, in phased-array antenna systems, amplitude tapering across the array aperture is employed to suppress side lobes. Inspired by these strategies, modified grating profiles such as sinusoidal and trapezoidal gratings have been explored[36-38]. However, these continuous-profile approaches pose significant fabrication challenges at nanometer scales[39] and do not completely eliminate secondary peaks, as residual side-lobe interference remains a limiting factor.

In this paper, we propose a binarized cosine-window grating that retains the sidelobe suppression characteristics of a continuous cosine window while being fully compatible with standard binary lithographic fabrication processes. We theoretically demonstrate its capability to suppress secondary diffraction peaks using Huygens–Fresnel diffraction theory, and construct an experimental platform based on a spatial light modulator to validate the approach in the visible regime. The experimental results agree well with theoretical predictions, confirming the effectiveness of the proposed design. Furthermore, numerical simulations across the soft X-ray wavelength range demonstrate that the suppression effect is preserved, indicating the method's applicability to practical X-ray spectroscopic systems. This approach provides a fabrication-friendly and effective method for improving grating performance in the X-ray regime.

2. Theoretical Model

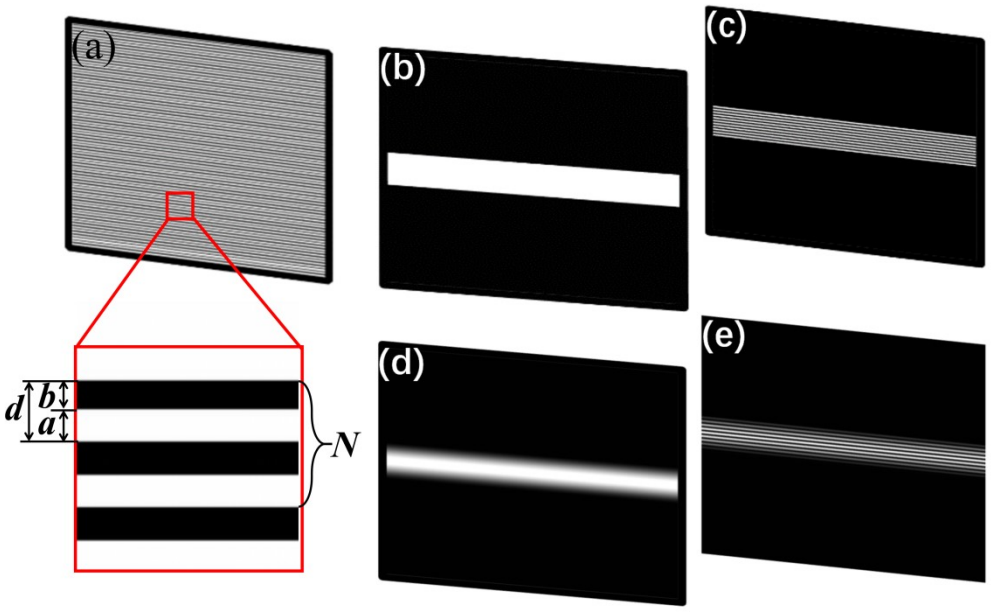


Fig. 1. (a) A binary amplitude TG of infinite width, (b) Rectangular window, (c) Binary amplitude TG truncated by a rectangular window, (d) Cosine window, (e) Binary amplitude TG truncated by a cosine window. The magnified inset illustrates the grating structural parameters: grating period *d*, slit width *a*, opaque bar width b and total strip number *N*.

The conventional TG is a one-dimensional amplitude grating with a binary periodic structure, as shown in Fig.1(a). Let a denote the slit width and d the grating period. Here, the grating period d represents the center-to-center distance between adjacent slits and satisfies d=a+b, where b is the width of the opaque bar between neighboring slits. The transmittance function of an ideal infinite grating is

$$t(x)=\begin{cases}1 & for\ nd < x \le a+nd \\ 0 & for\ nd+a < x \le (n+1)d\end{cases} \quad (n \in Z). \tag{1}$$

In practice, a rectangular window is applied to truncate the grating to a finite aperture, as demonstrated in Fig. 1(b). As a result, a binary amplitude grating TG with a finite width is obtained, which is presented in Fig. 1(c). Alternatively, a cosine window can be applied to introduce a smoothly varying transmittance profile along the transverse direction, as exhibited in Fig. 1(d), thereby yielding a binary amplitude grating with a cosine window restriction (Fig. 1(e)). The infinite grating is truncated by a rectangular window or modulated by a cosine window. The cosine window's gradual transmittance decay suppresses abrupt phase changes, redistributing energy from secondary peaks to the principal maxima via destructive interference. Since many practical situations do not satisfy the Fraunhofer diffraction, we use the Huygens-Fresnel diffraction formula for the calculations.

For a rectangular window of width *Nd*, the transmittance is

$$T_s(x)=\begin{cases}1 & for -\dfrac{Nd}{2}\le x\le \dfrac{Nd}{2}\\ 0 & otherwise\end{cases} \tag{2}$$

where d is the grating period and N is the number of periods. The diffracted intensity is calculated via the Huygens–Fresnel integral:

$$I_s(\xi)=\left|\frac{A}{j\lambda}\int_{-\frac{Nd}{2}}^{\frac{Nd}{2}} exp\left(\frac{2\pi jr}{\lambda}\right)dx\right|^2 \tag{3}$$

where ξ is the observation plane coordinate, x is the grating plane coordinate, $r=\sqrt{(x-\xi)^2+L^2}$, and L is the propagation distance.

Besides, the cosine window transmittance and corresponding diffracted intensity are:

$$T_c(x)=\begin{cases}\dfrac{1}{2}\left[1+\cos\left(\dfrac{2\pi x}{Nd}\right)\right] & for -\dfrac{Nd}{2}\le x\le \dfrac{Nd}{2}\\ 0 & otherwise\end{cases} \tag{4}$$

$$I_c(\xi)=\left|\frac{A}{j\lambda}\int_{-\frac{Nd}{2}}^{\frac{Nd}{2}}\frac{1}{2}\left[1+cos\left(\frac{2\pi x}{Nd}\right)\right]exp\left(\frac{2\pi jr}{\lambda}\right)dx\right|^2. \tag{5}$$

To quantitatively explain the sidelobe suppression mechanism, the Fourier transforms of the two window functions is analyzed. In the far-field diffraction regime, the intensity distribution of a windowed grating can be understood as the convolution of the discrete diffraction orders with the Fourier transform of the window function. Therefore, the secondary maxima between principal orders originate from the sidelobes of the window's Fourier spectrum.

For the rectangular window $T_s(x)$ defined in Eq. (2), the Fourier transform is:

$$T_s(f_x)=Nd\cdot\sin c(Ndf_x) \tag{6}$$

where sinc(u) = sin(πu)/(πu). The sidelobe envelope of the sinc function decays as ~1/f, with the first sidelobe level at approximately −13.3 dB relative to the main lobe.

For the cosine window $T_c(x)$ defined in Eq. (4), expanding the cosine term using Euler's formula yields three frequency-shifted rectangular components. Their Fourier transforms combine to give:

$$T_c(f_x)=\frac{Nd\cdot\sin(\pi Ndf_x)}{2\pi Ndf_x\cdot\left(1-N^2d^2{f_x}^2\right)} \tag{7}$$

For $Ndf_x\gg$, the denominator scales as $(Ndf_x)^3$, so the sidelobe envelope decays as $1/f_x^3$, which is two orders faster than that of the rectangular window. The first

sidelobe is suppressed to approximately −31.5 dB, representing an 18.2 dB improvement over the rectangular case.

This accelerated sidelobe decay is the quantitative origin of the secondary peak suppression observed in the simulations and experiments. Although the cosine window broadens the main lobe of each diffraction order by a factor of two, expanding its width from 2/Nd to 4/Nd, this modest resolution penalty is far outweighed by the dramatic sidelobe suppression, which is critical for resolving weak spectral features adjacent to strong diffraction orders. Moreover, in typical experimental configurations the effective resolution is further limited by detector pixel size, optical aberrations, and finite source bandwidth, so the additional broadening introduced by the apodization window is often a secondary effect rather than the dominant resolution-limiting factor.

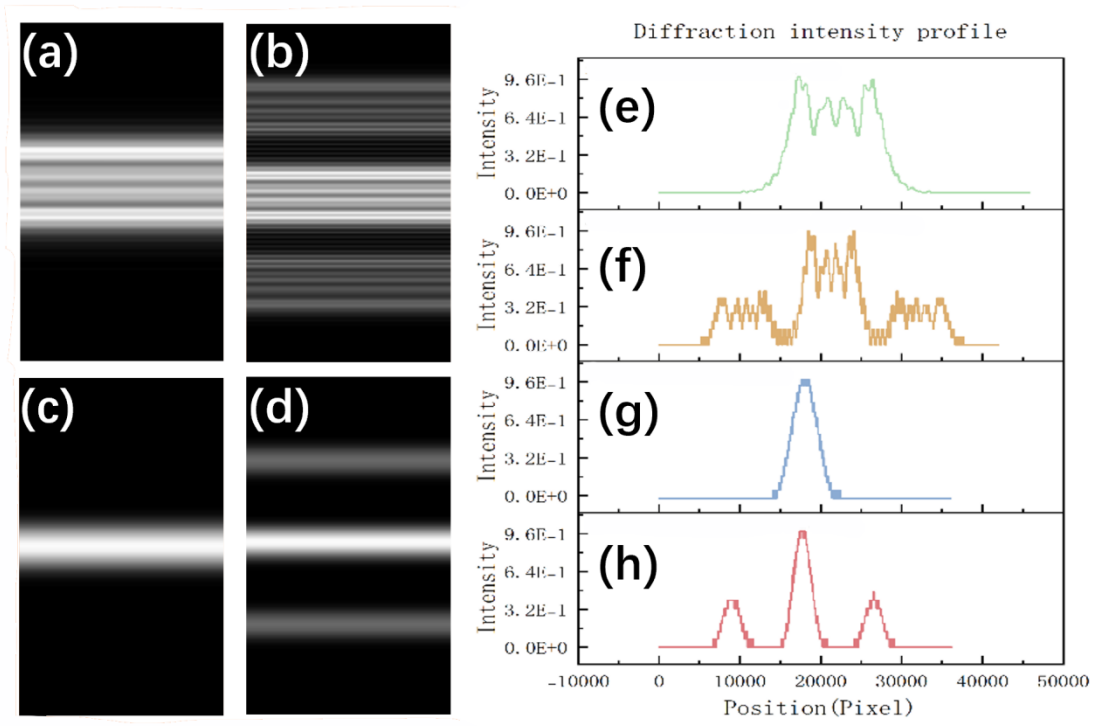


Fig.2. Simulated diffraction results ($a = 65\ \mu m$, $d = 130\ \mu m$, $N = 10$, $\lambda = 635\ nm$, $L = 1\ m$). (a)–(b) Two-dimensional diffraction patterns of the rectangular window alone and the rectangular-windowed grating, respectively. (c)–(d) Same as (a)–(b) but for the cosine window. (e)–(h) Corresponding cross-sectional intensity profiles for (a)–(d).

Fig. 2 shows simulated diffraction patterns for rectangular and cosine windows with parameters $a = 65\ \mu m$, $d = 130\ \mu m$, $N = 10$, $\lambda = 635\ nm$ and $L = 1\ m$. For the rectangular window, as shown in Fig. 2(a) the two-dimensional diffraction pattern of the window alone exhibits a broad sinc-like envelope. And when combined with the grating (Fig. 2(b)), pronounced secondary peaks appear between principal maxima due to sidelobe interference. The corresponding cross-sectional intensity profiles were shown in Fig 2(e) and 2(f), respectively, which reveal multiple secondary maxima

with intensities on the order of several percent of the principal peaks, introducing spectral contamination that degrades measurement accuracy. In contrast, as shown in Fig. 2(c), the cosine window produces a smoother two-dimensional diffraction envelope, characterized by significantly reduced sidelobe amplitudes. When applied to the grating shown in Fig. 2(d), the diffracted energy is redistributed toward the principal maxima. And the cross-sectional profiles (Fig. 2(g) and 2(h)) show that secondary peaks are suppressed to near-background levels while the principal peaks become noticeably sharper and more symmetric. A direct comparison between Fig. 2(f) and Fig. 2(h) clearly confirms the suppression of secondary maxima and the narrowing of principal peak widths achieved by the cosine window.

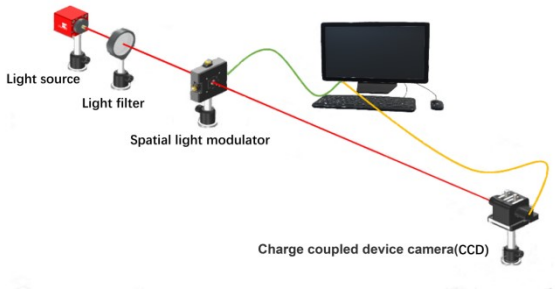


Fig.3. Schematic of the experimental setup.

3. Experimental arrangement, simulation and experiment.

To validate the theoretical model, a series of experiments were conducted using the setup shown in Fig. 3. A standard binary amplitude grating was designed with $a_1 = 65\ \mu m$, $d_1 = 130\ \mu m$, and $N_1 = 10$, as depicted in Fig. 4(a), which is equivalent to applying a rectangular window of finite width. Subsequently, a cosine window of limited width was added based on the black and white grating in conjunction with Eq. (4), as illustrated in Fig. 4(b). Experiments were carried out according to the experimental optical path constructed in Fig. 3. A λ=635 nm laser theodolite served as the beam source, along with a spatial light modulator capable of importing a two-dimensional grating and a visible Charge Coupled Device (CCD) for receiving the beam source signal. Eventually, the diffraction patterns in Fig. 4(c) and Fig. 4(d) were obtained on the CCD control software. As indicated by the labeled diffraction orders in Fig. 4(d), the 0th, +1st, and −1st orders are clearly resolved under the cosine window, with the secondary diffraction peaks effectively suppressed and each principal maximum conspicuously narrowed. In contrast, the rectangular-window diffraction pattern in Fig. 4(c) exhibits pronounced secondary peaks between the principal orders, making individual diffraction orders difficult to distinguish unambiguously.

To further substantiate the theoretical model, comparative experiments were performed using a sinusoidal grating. A rectangular window and a cosine window of finite width were respectively applied to the sinusoidal grating, whose transmittance varies sinusoidally within each period. The grating parameters were set to

$a_2 = 130\ \mu m$, $d_2 = 260\ \mu m$, $N_2 = 10$. A rectangular window and a cosine window of finite width were respectively applied, as shown in Fig. 4(e) and 4(f), while the corresponding diffraction patterns obtained using the experimental setup in Fig. 3 were presented in Fig. 4(g) and 4(h). Similarly, the 0th and ±1st diffraction orders are labeled in Fig. 4(h), where the cosine window produces clearly separated principal maxima with effectively suppressed secondary peaks. By comparison, the rectangular-window pattern in Fig. 4(g) shows substantial secondary peak contamination that obscures the boundaries between adjacent diffraction orders. Theoretically, the combination of a sinusoidal grating and a cosine window can eliminate higher-order interference, resulting in a diffraction spectrum with an ideal one-to-one correspondence with the incident wavelength. Although the experimental light source is not perfectly collimated, and minor deviations exist, these do not affect the overall conclusions, thereby confirming the effectiveness of the cosine window in improving grating diffraction performance.

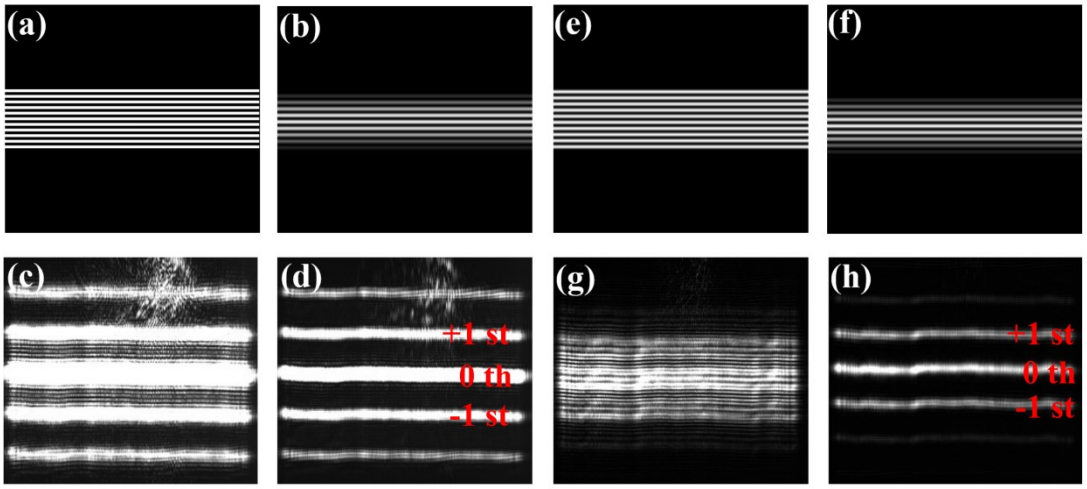


Fig.4. TG structures and corresponding experimental diffraction patterns. (a)–(b) Binary amplitude grating without and with cosine-window. (c)–(d) Measured diffraction patterns corresponding to (a) and (b). (e)–(f) Sinusoidal grating with rectangular and cosine windows. (g)–(h) Measured diffraction patterns corresponding to (e) and (f).

In practical fabrication, continuous cosine transmittance profiles with smooth gradients are challenging to realize at the nanoscale, where fabrication errors significantly limit applicability in the soft X-ray regime. To address this, we introduce a binarized cosine window that is compatible with standard lithographic processes while retaining the desired apodization characteristics. Visible-light experiments validate this approach, as shown in Fig. 4(h). The analytical treatment of the grating transmittance under a binarized cosine window is nontrivial. However, by exploiting the convolution property between an arbitrary function and an impulse lattice, the overall transmittance function $T(x, y)$ of the grating can be expressed as the

convolution of the transmittance function $t_1(x,y)$ of the short slit and the transmittance function $t_2(x,y)$ of the lattice as follows:

$$T(x,y) = t_1(x,y) * t_2(x,y) \tag{8}$$

According to Eq. (8), the binarized cosine windows of different periods can be obtained by convolution of lattice with short slit with different periods.

For comparison, a conventional binary amplitude TG with the same period was employed, as shown in Fig. 5(a), while the corresponding structure under the binarized cosine window is presented in Fig. 5(b). The grating parameters were set to $a_3 = 130\ \mu m$, $d_3 = 260\ \mu m$, $N_3 = 10$. The simulated diffraction pattern of the conventional grating, shown in Fig. 5(c), exhibits pronounced secondary diffraction features surrounding the principal maxima. In contrast, it can be seen from Fig. 5(d) that the simulated result for the grating under the binarized cosine window shows a significant redistribution of diffracted energy, with reduced side lobes and enhanced concentration in the principal diffraction orders.

Experimental results further confirm this behavior. As shown in Fig. 5(e), the measured diffraction pattern of the conventional binary amplitude TG displays noticeable secondary diffraction peaks and a broader intensity distribution, consistent with the simulation. By comparison, the experimental result for the TG with the binarized cosine window, shown in Fig. 5(f), demonstrates clear suppression of secondary peaks and a more localized intensity distribution around the principal maxima. The agreement between simulation and experiment verifies that the binarized cosine window effectively mitigates secondary diffraction effects while preserving the primary diffraction characteristics. This approach therefore provides a practical and robust solution for improving diffraction performance in realistic optical systems. For the case without the cosine window, the diffraction spectrum was analyzed in the region of the secondary diffraction peaks by repeatedly measuring the light intensity $I_{i,1}$ (i=1,2,…,n). The signal intensity S_1 was then obtained by averaging these measurements as follows:

$$S_1 = \frac{1}{n}\sum_{i=1}^{n} I_{i,1}. \tag{9}$$

Meanwhile, the noise intensity N_1 is approximated by calculating the standard deviation of these data with the following equation:

$$N_1 = \sqrt{\frac{1}{n-1}\sum_{i=1}^{n}\left(I_{i,1} - S_1\right)^2}\,. \tag{10}$$

From this, the signal-to-noise ratio SNR_1 of the secondary diffraction peak without the cosine window can be expressed as:

$$SNR_1 = \frac{S_1}{N_1}\,. \tag{11}$$

Similarly, the signal-to-noise ratio SNR_2 of the secondary diffraction peak with the addition of a cosine window is obtained as:

$$SNR_2 = \frac{S_2}{N_2}\,. \tag{12}$$

The signal-to-noise ratio is improved by approximately 27.36 dB. On the observation plane, a CCD located at a distance z from the transmission grating records the light field distribution $U(x,y,z)$, which can be approximated as follows:

$$U(x,y,z) = \frac{exp^{ikz}}{i\lambda z}\iint_{-\infty}^{\infty} U_0(\xi,\eta)\, exp^{\frac{ik}{2z}\left[(x-\xi)^2+(y-\eta)^2\right]} d\xi d\eta \tag{13}$$

where $k = \dfrac{2\pi}{\lambda}$ is the wave number, λ is the wavelength of light, $U_0(\xi,\eta)$ is the complex amplitude distribution on the grating plane, (ξ,η) are the coordinates of the grating plane and (x,y) are the coordinates of the observation plane.

The light intensity $I_r(x,y)$ in the region of the secondary diffraction peaks is integrated to obtain the integrated intensity I_{r-int}, which is calculated as:

$$I_{r-int} = \iint_A I_r(x,y)\,dxdy\,. \tag{14}$$

Here the integration region A is the region where the selected secondary diffraction peaks are located. When the cosine window is added to the transmission grating, the complex amplitude distribution on the grating plane becomes $U_1(\xi,\eta)$, which is equal to the product of $U_0(\xi,\eta)$ and the cosine function, i.e.

$U_1(\xi,\eta)=U_0(\xi,\eta)\cdot C(\xi,\eta)$, where $C(\xi,\eta)$ is the cosine window function. The light field distribution $U_2(x,y,z)$ on the observation plane is calculated again according to the Fresnel diffraction formula, and the light intensity distribution $I_c(x,y)$ is obtained. The light intensity in the region of the selected secondary diffraction peaks is also integrated to obtain the integrated intensity I_{c-int} with the addition of the cosine window, calculated as:

$$I_{c-int}=\iint_A I_c(x,y)\,dxdy. \tag{15}$$

In order to present a clear picture of the extent to which the addition of a cosine window affects the intensity of the secondary diffraction peaks, we calculate the proportion ΔI of the intensity change with the following:

$$\Delta I=\frac{I_{r-int}-I_{c-int}}{I_{r-int}}\times 100\%. \tag{16}$$

Through the above measurements and calculations based on the Fresnel diffraction theory, the intensity of the secondary diffraction peaks of the grating under the cosine window is reduced by about 93.12% compared with that of the rectangular window grating, which proves that the cosine window has an obvious suppression effect on the secondary diffraction peaks.

4. **Result and discussion**

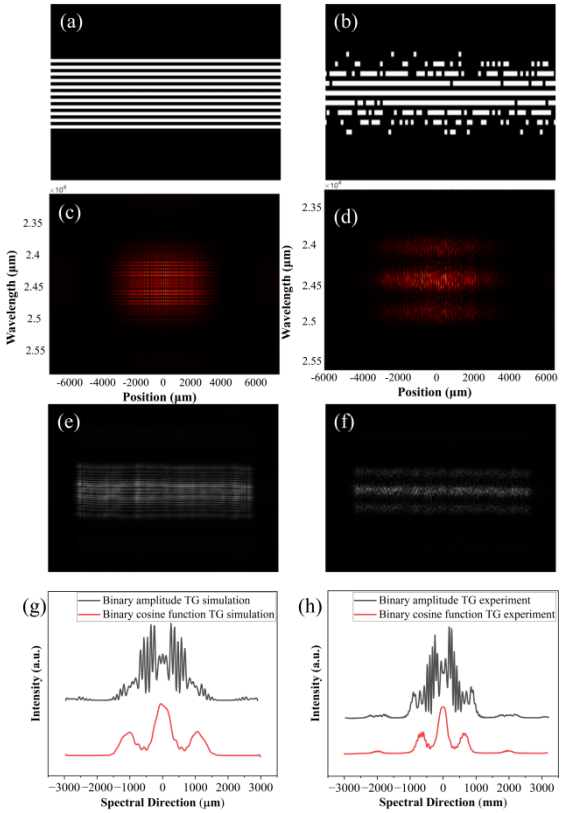


Fig.5. Comparison of conventional and binarized cosine window gratings. (a) The TG structure of conventional binary amplitude TG, (b) The TG structure of binarized cosine window grating, (c)–(d) Simulated diffraction patterns for (a) and (b), (e)–(f) Experimental diffraction patterns for (a) and (b), (g) Simulated and experimental cross-sectional intensity profiles extracted from (c) and (e), (h) Simulated and experimental cross-sectional intensity profiles extracted from (d) and (f).

Substituting the abrupt step change in the cosine function with its binarized counterpart remarkably augments the usability of TGs across diverse optical regions, and this is especially true in the X-ray spectrum. This binarization provides a higher level of tolerance towards the imperfections that might crop up during the actual production and manufacturing procedures. Based on our analysis of the experimental results, we have managed to determine the diffraction intensity distribution. Whether the diffraction patterns are obtained from computer simulations or actual experiments, the advantages of employing a binarized cosine window are quite apparent. The intensity distributions depicted in Fig. 5(g) and Fig. 5(h) correspond respectively to those in Fig. 5(c)-(f). It has been found that the positions and intensities of each peak are largely in line with one another. The binarized cosine window evidently alleviates the impacts of the sidelobe artifacts that are commonly associated with rectangular windows. As a result, smoother transitions are achieved between individual diffraction peaks, which bolsters the overall clarity and performance of the gratings. Such an improvement is especially advantageous for applications that demand high precision and a reduction in noise within the diffraction patterns.

In the preceding simulations, the opaque bar regions were modeled as perfectly absorbing with zero transmittance. While this is a valid approximation in the visible

regime, it does not hold in the soft X-ray range, where all materials exhibit finite absorption and introduce phase shifts due to the complex refractive index $n=1-\delta-i\beta$. To assess the impact of realistic material properties on the suppression performance, we performed additional simulations incorporating the optical constants of gold.

At λ=0.15 nm, the optical constants obtained from the CXRO Henke database[40] are $\delta=4.4618\times10^{-5}$ and $\beta=4.4041\times10^{-6}$. The transmittance function of the grating under realistic material conditions can be written as[41]

$$\tilde{\quad}\quad\tilde{\quad}\quad\tilde{\quad}\quad\cdot i(2\pi\delta/\lambda)\tau]\times\exp[-(2\pi\beta/\lambda)\tau] \tag{17}$$

where $\tilde{}$ is the ideal binary transmittance function of the binarized cosine window grating , τ is the gold bar thickness, and δ and β are the real and imaginary parts of the refractive index decrement obtained from the CXRO Henke database. The first term represents the unattenuated transmission through the open slits, while the second term accounts for the residual transmission through the gold bars with both amplitude attenuation and phase shift.

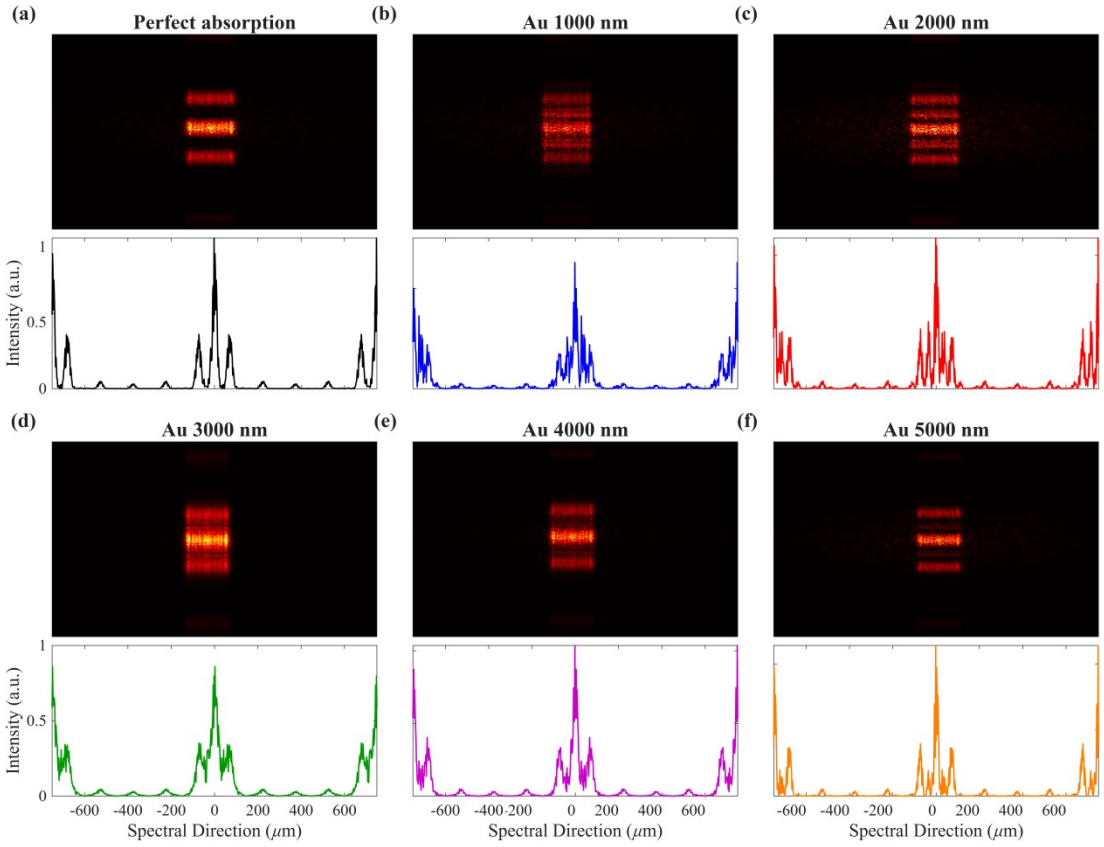


Fig. 6. Effect of finite gold bar absorption on diffraction performance of the binarized cosine window grating at λ= 0.15 nm. (a) Ideal perfect-absorption model. (b)–(f) Realistic model incorporating the

complex refractive index of gold with bar thicknesses of τ= 1000, 2000, 3000, 4000, and 5000 nm, respectively. Upper panels: two-dimensional diffraction patterns. Lower panels: cross-sectional intensity profiles along the spectral direction.

Fig.6 presents a systematic comparison of the diffraction intensity distributions for the binarized cosine window grating under different gold thicknesses: τ=1000, 2000, 3000, 4000, and 5000 nm, alongside the ideal perfect-absorption case with $a = 0.5\ \mu m$, $d = 1\ \mu m$, $L = 0.4\ m$, $N = 500$. For τ= 1000 nm, the residual X-ray transmission through the gold bars is non-negligible, and the resulting diffraction pattern exhibits slightly elevated background intensity and weakly enhanced secondary peaks compared to the ideal case. As τ increases to 2000–3000 nm, the amplitude attenuation becomes sufficient to suppress most of the transmitted flux, and the diffraction patterns converge toward the perfect-absorption result. For τ≥4000 nm, the diffraction profiles are essentially indistinguishable from the ideal model.

These results demonstrate two important conclusions. First, the fundamental sidelobe suppression mechanism of the cosine window, which arises from the destructive interference among three frequency-shifted sinc components in the Fourier domain, is preserved under realistic material conditions. The finite absorption and phase shift modify the absolute intensity but do not alter the underlying apodization principle. Second, the required gold thickness for effective X-ray operation is well within the range achievable by current nanofabrication processes. For X-rays at 8 keV, a gold thickness of 3–5 μm provides absorption contrast exceeding 99%, ensuring that the binarized cosine window grating performs as designed. For lower photon energies in the soft X-ray regime (0.1–2 keV), the absorption coefficient β is generally larger, which means that thinner gold films can achieve comparable attenuation.

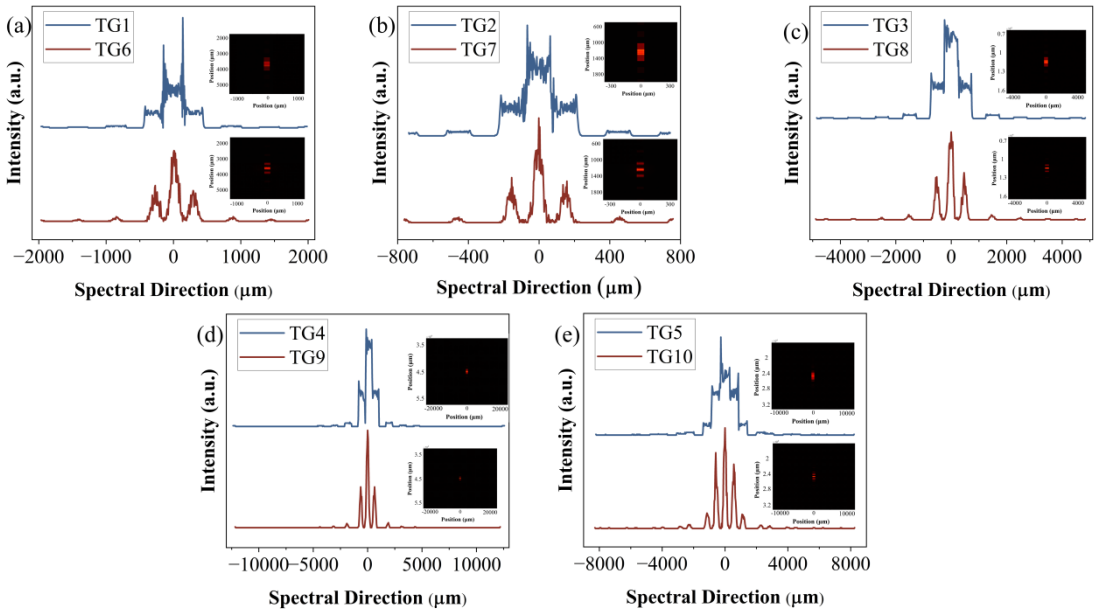


Fig.7. Simulated diffraction intensity profiles of binary amplitude TG and Binarized cosine window TG for soft X-ray wavelength (a) 0.15 nm, (b) 0.5 nm, (c) 2 nm, (d) 5 nm and (e) 10 nm. Insets show the diffraction patterns.

The diffraction patterns of the binary amplitude TG and the sinusoidal grating clearly show that the use of the cosine window greatly reduces the intensity of the secondary diffraction peaks. Experimental results show that our proposed technique can improve the spectral resolution and signal-to-noise ratio, thus validating its effectiveness. Building upon the experimental validation in the visible regime, we now examine the theoretical implications for X-ray applications. On top of that, we also simulated the diffraction of the TG and the TG with a binarized cosine window with $a = 0.5\ \mu m$, $d = 1\ \mu m$, $L = 0.4\ m, N = 500$ as shown in Fig. 7, which shows that the secondary diffraction peaks are suppressed effectively across all wavelengths. The simulated parameters is shown in Table.1. It can be seen from the pictures that our proposed technique can improve the spectral resolution and reduce spectral interference, which is of great significance for improving the accuracy of spectral measurements. The ability of the cosine window to refine the diffraction pattern can play a key role in achieving higher accuracy in spectral analysis, which is a key factor in promoting the progress of diffraction spectroscopy research and the optimization of optical systems. Visible-light experiments achieve 93.12% suppression of secondary peaks, while 8 keV simulations show 84% reduction. This consistency validates the method's applicability to soft X-ray spectroscopy.

Table.1. Simulated parameters for grating diffraction measurements.

NO.	Slit width a (μm)	Grating period d (μm)	Distance from the grating to the recording plane L (m)	Grating period number N	Light source wavelength λ (nm)	TG type
TG1	0.5	1	0.4	500	0.15	Binary amplitude
TG2	0.5	1	0.4	500	0.5	Binary amplitude
TG3	0.5	1	0.4	500	2	Binary amplitude
TG4	0.5	1	0.4	500	5	Binary amplitude
TG5	0.5	1	0.4	500	10	Binary amplitude
TG6	0.5	1	0.4	500	0.15	Binarized cosine window
TG7	0.5	1	0.4	500	0.5	Binarized

						cosine window
TG8	0.5	1	0.4	500	2	Binarized cosine window
TG9	0.5	1	0.4	500	5	Binarized cosine window
TG10	0.5	1	0.4	500	10	Binarized cosine window

5. Conclusion

In summary, we present a practical approach for suppressing secondary diffraction peaks in transmission gratings by introducing a cosine window and its binarized implementation. Theoretical analysis, numerical simulations, and visible-light experiments consistently demonstrate that this design effectively redistributes diffracted energy from secondary peaks into the principal maxima. As a result, a substantial reduction of 93.12% in secondary peak intensity and an improvement of approximately 27.36 dB in signal-to-noise ratio are achieved, leading to enhanced spectral resolution and measurement reliability. The binarized cosine window further ensures compatibility with realistic fabrication processes, particularly in the soft X-ray regime, while maintaining strong suppression performance. These results indicate that the proposed method provides a viable alternative to conventional rectangular-window gratings and offers a robust strategy for improving diffraction quality. This approach is expected to benefit high-precision spectroscopic diagnostics and advance applications in areas such as high energy density physics and advanced materials research.

Acknowledgment

Project supported by the Natural Science Foundation of China (12405247); Natural Science Foundation of China (12475238); Outstanding Talents Training Fund in Shenzhen (202101) and Guangdong Provincial Department of Young Innovative Talents Project (2024KQNCX038).

References

[1] Sinha S, Jeyaseelan C, Singh G, Munjal T and Paul D 2023 Basic Biotechniques for Bioprocess and Bioentrepreneurship, Bhatt A K, et al. eds. (London: Academic Press) pp. 145-164

[2] Kutner M L 2003 Astronomy: A Physical Perspective, 2 edn. (Cambridge:

Cambridge University Press)
[3] Tennyson J 2019 Astronomical Spectroscopy: An Introduction to the Atomic and Molecular Physics of Astronomical Spectroscopy (Singapore: World Scientific Publishing)
[4] Sibilia J P 1988 A Guide to Materials Characterization and Chemical Analysis (New York)
[5] Wang J, Ma Q, Wang Y, Li Z, Li Z and Yuan Q 2018 Chemical Society Reviews 47 8766
[6] Chapman D V 1996 Water Quality Assessments: A Guide to the Use of Biota, Sediments and Water in Environmental Monitoring (London: CRC Press)
[7] Yao J, Yang M and Duan Y 2014 Chemical Reviews 114 12 6130
[8] Canizares C R, Davis J E, Dewey D, Flanagan K A, Galton E B, Huenemoerder D P, Ishibashi K, Markert T H, Marshall H L, McGuirk M, Schattenburg M L, Schulz N S, Smith H I and Wise M 2005 Publications of the Astronomical Society of the Pacific 117 1144
[9] Brinkman A C, Gunsing C J T, Kaastra J S, van der Meer R L J, Mewe R, Paerels F, Raassen A J J, van Rooijen J J, Bräuninger H, Burkert W, Burwitz V, Hartner G, Predehl P, Ness J U, Schmitt J, Drake J J, Johnson O, Juda M, Kashyap V, Murray S S, Pease D, Ratzlaff P and Wargelin B J 2000 Astrophysical Journal 530 L111
[10] Lindl J D, Amendt P, Berger R L, Glendinning S G, Glenzer S H, Haan S W, Kauffman R L, Landen O L and Suter L J 2004 Physics of Plasmas 11 339
[11] Sander D and Müller J 2001 Sensors and Actuators A-Physical 88 1
[12] Johnsen S 2011 The Optics of Life: A Biologist's Guide to Light in Nature (Princeton: Princeton University Press)
[13] Wellburn A R 1994 Journal of Plant Physiology 144 307
[14] Attwood D 1999 Soft X-Rays and Extreme Ultraviolet Radiation: Principles and Applications (Cambridge: Cambridge University Press)
[15] Pimpin A and Srituravanich W 2012 Engineering journal 16 37
[16] Chergui M, Beye M, Mukamel S, Svetina C and Masciovecchio C 2023 Nature Reviews Physics 5 578
[17] Bonod N and Neauport J 2016 Advances in Optics and Photonics 8 156
[18] Xie Y, Zakharian A R, Moloney J V and Mansuripur M 2004 Optics Express 12 6106
[19] Seo M, Adam A, Kang J, Lee J, Jeoung S, Park Q, Planken P and Kim D 2007 Optics Express 15 11781
[20] Gaylord T K and Moharam M 1985 Proceedings of the IEEE 73 894
[21] Bracewell R 2012 Fourier analysis and imaging (Springer Science & Business Media)
[22] Luo X, Tsai D, Gu M and Hong M 2018 Advances in Optics and Photonics 10 757
[23] Angelo J P, Chen S-J, Ochoa M, Sunar U, Gioux S and Intes X 2019 Journal of biomedical optics 24 071602
[24] He B B 2018 Two-dimensional X-ray Diffraction (Chichester: John Wiley & Sons)

[25] Labeyrie A, Lipson S G and Nisenson P 2006 An introduction to optical stellar interferometry (Cambridge: Cambridge University Press)
[26] Levkivskyi I P and Sukhorukov E V 2008 Physical Review B—Condensed Matter and Materials Physics 78 045322
[27] Derode A, Tourin A and Fink M 2001 Physical Review E 64 036606
[28] Rischel C, Rousse A, Uschmann I, Albouy P-A, Geindre J-P, Audebert P, Gauthier J-C, Fröster E, Martin J-L and Antonetti A 1997 Nature 390 490
[29] Bacon C P, Mattley Y and DeFrece R 2004 Review of Scientific instruments 75 1
[30] Griem and Hans R 1998 Nuclear Fusion 38 1255
[31] Nagayama T, Bailey J E, Loisel G P, Dunham G S, Rochau G A, Blancard C, Colgan J, Cossé P, Faussurier G, Fontes C J, Gilleron F, Hansen S B, Iglesias C A, Golovkin I E, Kilcrease D P, MacFarlane J J, Mancini R C, More R M, Orban C, Pain J C, Sherrill M E and Wilson B G 2019 Physical Review Letters 122 235001
[32] Palmer C and Loewen E G 2005 Diffraction grating handbook (New York: Richardson Grating Laboratory)
[33] Hansen R C 2009 Phased array antennas (Chichester: John Wiley & Sons)
[34] Harris F J 1978 Proceedings of the IEEE 66 51
[35] Oppenheim A V and Schafer R W 2009 Discrete-Time Signal Processing (Upper Saddle River: Prentice Hall Press)
[36] Zang H, Cui Z, Wei L, Liu H, Fan Q, He Y, Sun B, Chen J and Cao L 2023 Photonics 10 3, p. 303
[37] Yang Z, Fan Q, Li P, Wei L, Zhang Q, Chen Y, Wu Y, Wang S and Cao L 2018 AIP Advances 8 125331
[38] Cao L, Förster E, Fuhrmann A, Wang C, Kuang L, Liu S and Ding Y 2007 Applied Physics Letters 90 5
[39] Heilmann R K, Davis J E, Dewey D, Bautz M W, Foster R, Bruccoleri A, Mukherjee P, Robinson D, Huenemoerder D P, Marshall H L, Schattenburg M L, Schulz N S, Guo L J, Kaplan A F and Schweikart R B 2010 Conference on Space Telescopes and Instrumentation 2010 - Ultraviolet to Gamma Ray, Jun 28-Jul 02,2010, San Diego, CA
[40] Henke B L, Gullikson E M and Davis J C 1993 Atomic Data and Nuclear Data Tables 54 181
[41] Zang H P, Wang C K, Gao Y L, Zhou W M, Kuang L Y, Wei L, Fan W, Zhang W H, Zhao Z Q, Cao L F, Gu Y Q, Zhang B H, Jiang G, Zhu X L, Xie C Q, Zhao Y D and Cui M Q 2012 Applied Physics Letters. 100 111904